Applied Surface Science 648 (2024) 158962

Contents lists available at ScienceDirect

Applied Surface Science

journal homepage: www.elsevier.com/locate/apsusc

Full Length Article

Room-temperature solid-state metallic lithium batteries based on high-content boron nitride nanosheet-modified polymer electrolytes

Xianglong Meng, Dongmei Zhang, Jinshan Mo, Lehao Liu *, Tianrong Yang, Qianxiao Fan, Qian Zhao, Rongmin Zhou, Mengxuan Zhang, Wenyan Hou, Weihao Hu, Wendi Zhang, Yilong Jin, Bing Jiang, Lihua Chu, Meicheng Li *

State Key Laboratory of Alternate Electrical Power System with Renewable Energy Sources, School of New Energy, North China Electric Power University, Beijing 102206, China

ARTICLE INFO

Keywords:
Metallic lithium battery
Boron nitride nanosheet
Composite solid electrolyte
High ionic conductivity

ABSTRACT

Polyethylene oxide (PEO)-based solid-state electrolytes have great potential in the development of solid-state metallic lithium batteries. However, it is difficult to apply them in metallic lithium batteries at room temperature because of the poor ionic conductivity and the lithium dendrite-induced safety problem. Herein, high-performance composite polymer electrolytes (CPEs) are developed by filling high-content boron nitride (BN) nanosheets with well dispersity in the PEO-LiTFSI matrices. Theoretical calculations and experimental characterizations reveal that the BN nanofillers with a strong Lewis acid property can capture $TFSI^-$ to release more free Li^+, reduce the polymer crystallinity, and facilitate the generation of rich BN/PEO-LiTFSI fast-ion interfaces. Thus, the ionic conductivity and the Li^+ transference number of the CPEs at room temperature greatly increase to 4 and 2 times those of the pristine electrolyte, respectively. Hence, the Li/CPE/Li batteries can operate steadily at 0.05 mA/cm^2 (0.05 mAh/cm^2) and 30 °C for 1200 h. Furthermore, the $LiFePO_4$/CPE/Li batteries show higher initial capacity of 132 mAh/g and capacity retention of 84 % after 90 cycles at 0.3C and 30 °C than the pristine electrolyte-based batteries (29 %). This study provides a feasible case to prepare excellent-performance CPE films containing high nanofiller content for room-temperature solid-state metallic lithium batteries.

1. Introduction

Lithium ion batteries play an important role in large-scale power grid energy storage, electric vehicles, portable electronics, aerospace and other fields [1,2]. In particular, using lithium metals as the anodes is a prospective option for high-energy–density batteries, because the specific capacity of the lithium metal electrode is ten times that of commonly-used graphite electrodes [3]. Unfortunately, the commercial liquid electrolytes pose combustion and explosion hazards, because the organic solvents are volatile and combustible, and the uncontrollable lithium dendrites are easy to puncture the separator membranes to induce the internal short circuit [4,5].

Distinguished from the conventional liquid electrolytes, solid-state electrolytes have better physical and chemical properties, which can fundamentally solve the leakage and inflammability problems. Moreover, solid-state electrolytes can function as separators, restraining the growth of the lithium dendrites and simplifying the battery assembly process [6]. In particular, solid polymer electrolytes (SPEs) have many advantages including easy film forming, good flexibility, simple preparation and low cost among all kinds of solid-state electrolytes. Polyethylene oxide (PEO) has excellent electrochemical stability, low price, high dielectric constant (~9), and strong dissociation ability of lithium salts, making it one of the most widely studied polymers for preparing SPEs [7–9]. However, the ionic conductivity of the PEO-based electrolytes is low (10^{-8} – 10^{-6} S cm^{-1} at room temperature) because of the high crystallinity and the poor chain migration ability [10,11]. Moreover, PEO-based electrolytes also have other disadvantages such as poor mechanical strength (~0.4 MPa), low Li^+ transference number (~0.2), narrow electrochemical window (~4.0 V) and insufficient dendrite inhibition ability, which all seriously hinder their practical application in room-temperature solid-state metallic lithium batteries [12–14].

Dispersing inorganic nanoparticles (e.g., Al_2O_3 and SiO_2) [15–17] into the polymer electrolytes is considered as an effective method to improve their comprehensive properties. Inorganic nanoparticles with

* Corresponding authors.
E-mail addresses: lehaoliu@ncepu.edu.cn (L. Liu), mcli@ncepu.edu.cn (M. Li).

https://doi.org/10.1016/j.apsusc.2023.158962
Received 25 September 2023; Received in revised form 12 November 2023; Accepted 19 November 2023
Available online 28 November 2023

Lewis acid-base properties can interact with lithium salts, which could promote the electrolyte salt dissociation to release free lithium ions, and meanwhile increase the amorphous regions, thereby improving the ionic conductivity of the SPEs [18–23]. Moreover, a large number of polymer/nanoparticle interfaces will form if doping the large specific surface area nanoparticles into the polymer electrolytes. Some characterizations revealed the existence of interfacial fast ion channels [24–27]. Therefore, doping nanoparticles with high specific surface areas has the potential to increase the interface area and prolong the fast ion transport path to further improve the ionic conductivity. In addition, filling nanoparticles can improve other properties such as electrochemical window, thermal stability and the lithium dendrite inhibition capability. Compared with 0D nanospheres and 1D nanofibers, 2D nanosheets (e.g., graphene oxide) have a large specific surface area to interact with the polymer, thus effectively improving the ionic conductivity of the SPEs [20,23,28]. A few special atoms or functional groups in the nanofillers can also effectively capture the anions to increase the Li^+ transference number [13,18,28], which is benefit to prevent the growth of lithium dendrite. While some articles have reported the 2D nanosheet-modified composite polymer electrolytes (CPEs) with improved properties, few given the application of PEO-based electrolytes in metallic lithium batteries at room temperature (usually 50–70 °C) [29]. Moreover, the large-surface-area nanofillers are prone to aggregate especially with high contents, and thus resulting in the deterioration of the electrolyte properties. A few methods such as in-situ synthesis of nanoparticles in electrolyte matrices [22] and modification coating of the nanoparticles [30] are often used to prevent the nanoparticles agglomerating in the polymer electrolytes. Nevertheless, their methods induce other issues such as the complicated preparation process, and the generation of new impurities.

Herein, a simple yet efficient method is utilized to disperse boron nitride (BN) nanosheets by sonicating and stirring the hydroxylated BN nanosheets in N-methylpyrrolidone (NMP) as solvent instead of the commonly-used acetonitrile (ACN). High-content (10 wt%) BN-filled CPE films with evenly-distributed BN nanosheets are then prepared by solution casting of the mixed PEO/LiTFSI/BN solution followed by drying in vacuum condition (Fig. 1a). Theoretical calculations and experimental measurements verify that the hydroxylated BN nanosheets with strong Lewis acid property can capture the $TFSI^-$ anions to promote the dissociation of lithium salt, and meanwhile inhibit the PEO crystallization (Fig. 1b). Moreover, abundant BN/PEO-LiTFSI interfaces can facilitate the ion transport, then strongly increasing the ionic conductivity and Li^+ transference number (Fig. 1c). The electrochemical stability, tensile property and thermostability are also enhanced by the high-content BN fillers. Most importantly, compared to the pristine PEO-LiTFSI electrolyte-based cells, the CPE-based solid-state metallic lithium batteries can inhibit the lithium dendrites and operate for a long time stably, and have a high capacity even under high charge–discharge rates at room temperature. This study provides an easy yet feasible modification method to realize comprehensively-updated polymer electrolytes with high nanofiller content for room-temperature all-solid-state metallic lithium batteries.

2. Experimental section

2.1. Preparation of BN nanosheet dispersion

0.278 g BN nanosheets (Nanjing XFNANO Materials Tech Co., Ltd) were added into 5 mL NMP (99.9 %, Innochem) and 5 mL ACN (99.8 %, Aladdin) solution, respectively, and then ultrasonicated for 30 min and stirred strongly for 24 h. The NMP dispersions containing 0.025, 0.132, 0.278, 0.410, 0.556 and 0.688 g BN nanosheets were also prepared for obtaining the CPEs with 1, 5, 10, 15, 20 and 25 wt% BN, respectively.

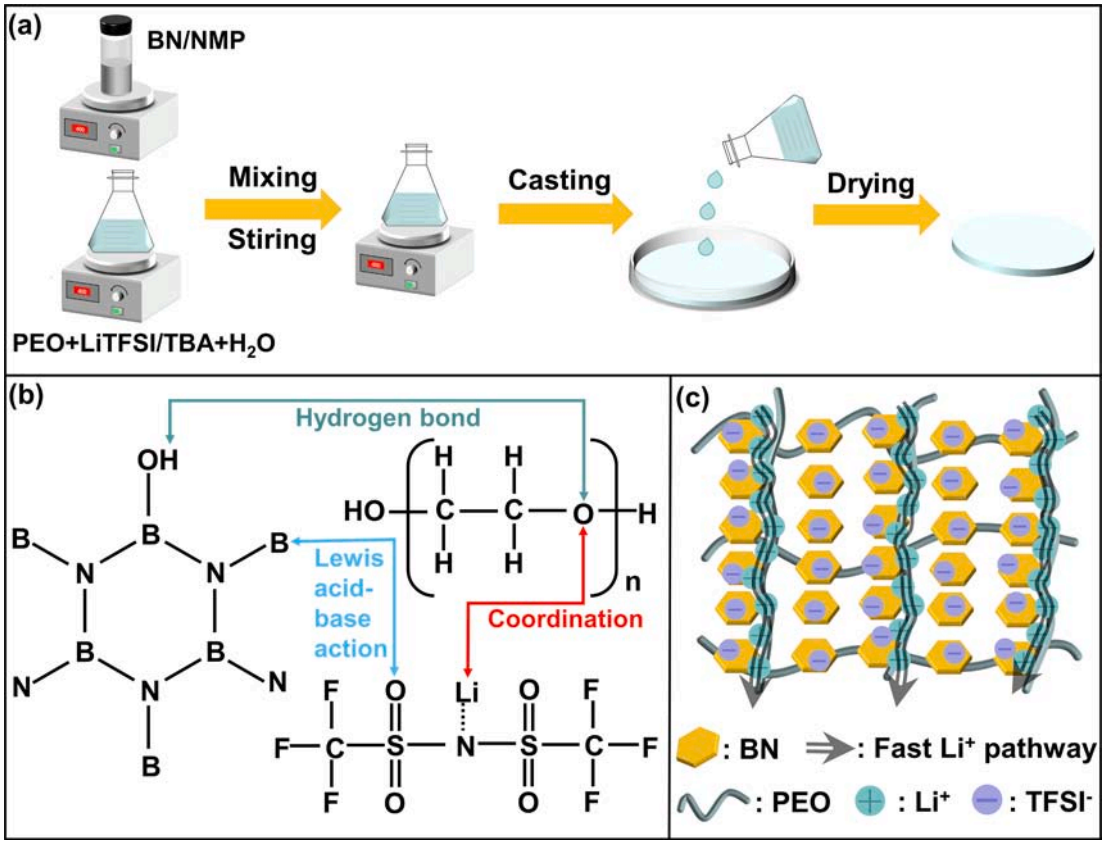

Fig. 1. (a) Schematic description of preparing the PEO-LiTFSI-BN CPE by solution casting method, (b) the interactions between PEO/LiTFSI and the BN nanosheets, and (c) the structure of the CPE.

2.2. Preparation of PEO-LiTFSI-BN CPEs

0, 0.025, 0.132 and 0.278 g BN nanosheets were added into 4 bottles containing 5 mL NMP solution, respectively, then ultrasonicated for 30 min and stirred strongly for 24 h. 1.835 g PEO (Sigma Aldrich, molecular weight: 600,000) and 0.665 g LiTFSI (99 %, Aladdin) (EO:Li^+=18:1) were dissolved in a mixture solution containing 10 mL *tert*-butanol (TBA) (99.5 %, Aladdin) and 21 mL deionized water, and then stirrd for 24 h. The BN dispersion solutions were then added into the PEO-LiTFSI solution and stirred for 24 h. The composite electrolyte solutions were then casted in Teflon molds and dried at 60 °C in vacuum for 72 h to evaporate the solvents. The CPE membranes containing 0, 1, 5, and 10 wt% BN were named as BN0, BN1, BN5 and BN10, respectively. The CPEs were cut into 19 mm diameter discs and stored in a glove box (H_2O: < 0.1 ppm, O_2: < 0.1 ppm) to evaporate the residual solvent completely.

2.3. Material characterizations

A Malvern Nano ZS90 nano size potential analyzer was used to test the size of BN nanosheets in the dispersing solvents. A FEI F20 field emission transmission electron microscope (TEM) was used to observe the microstructure and morphology of the BN nanosheets. A SU8010 field emission scanning electron microscope (SEM) combined with an energy dispersive spectroscope (EDS) was used to observe the surface and cross section morphology and element composition of the composite solid electrolytes with different BN contents. A JB-126A tensile tester was used to stretch the electrolyte film at 5 mm/min to test the mechanical tensile properties of the films. A D8 Focus X-ray diffractometer (XRD) was used to explore the effect of BN on the crystallinity of the SPEs. A D840TA Q500 thermogravimetric analyzer (TGA) was used to test thermogravimetric performance of BN nanosheets and SPEs in a nitrogen atmosphere at 10 °C /min. A Thermo Scientific Nicolet iS50 Fourier transform infrared (FT-IR) spectrometer was used to detect the functional groups and chemical bonds of the BN nanosheets, LiTFSI and SPEs. A Netzsch DSC 200 F3 differential scanning calorimeter (DSC) was used to test the crystallinity of the SPEs between − 90–110 °C. The crystallinity (χ) can be calculated according to the formula [14]:

$$\chi = (\Delta H/F{\cdot}\Delta H_0){\cdot}100\%$$

where ΔH was the enthalpy change of the SPEs, ΔH_0 was 213.7 J/g, representing the melting enthalpy of PEO, and F was the mass ratio of PEO in the films. A Bruker Avance Neo 400WB solid-state nuclear magnetic resonance (ssNMR) spectrometer was used to conduct ^{7}Li magic-angle spinning (MAS) with a Larmor frequency of 73.6 MHz. The resulting spectra were referenced to LiCl solution at 0 ppm [31].

2.4. DFT calculations and MD calculations

Density functional theory (DFT) was used to calculate the adsorption energy of BN on $TFSI^-$ and Li^+. The DFT calculations were performed using Gaussian16 software and VMD software for visualization, at the level of def2svp. The interaction relationship between $TFSI^-$ (Li^+) and BN is calculated by the following formula:

$$E_{interact-BN-TFSI^-(Li^+)} = E_{BN-TFSI^-(Li^+)} - E_{BN} - E_{TFSI^-(Li^+)}$$

Molecular dynamics (MD) simulations were used to calculate the diffusion of Li^+ and $TFSI^-$ in BN0 and BN10 systems. The size of the periodic simulation pool was 42 × 42 × 42 Å and 44 × 44 × 44 Å, respectively. PEO chain segment was formed by 20 EO monomers, and the initial position of each component was determined by the random number generator. Ten initial conformations were constructed for each model, and the conformations with lower energy among the ten configurations was selected as the more reasonable initial model. In order to obtain more reasonable kinetic results, the initial conformation structure was optimized firstly, and then the structure was subjected to annealing cycles of 300–500 K to ensure full relaxation of the structure. The Nose temperature control method was adopted to control the temperature at 298 K, and the cutoff radius was 12.5 Å. Then, the MD simulations were carried out under NPT ensemble for 800 ps. The pressure control mode was Berendsen. It was found that the cell density curves had reached dynamic equilibrium up 800 ps, and the mean square displacement (MSD) analysis was performed on the results. Frames containing Li^+ and $TFSI^-$ position information were output every 500 steps. All dynamics use COMPASS force fields to explain molecular interactions.

The diffusion coefficients of molecules in different systems can be estimated from the slope of the MSD curve using the Einstein relationship:

$$MSD(\Delta t) = \frac{1}{\tau - \Delta t}\int_0^{\tau-\Delta t}[r(t-\Delta t) - r(t)]^2 dt = \left\{[r(t-\Delta t) - r(t)]^2\right\}$$

2.5. Electrochemical measurements

Symmetric or asymmetric cells were prepared by loading the electrolytes into CR2032 coin cells for electrochemical characterization. A Zahner Zennium electrochemical workstation was utilized to test the impedance of the symmetrical stainless steel (SS)/SPE/SS batteries in the frequency between 10^6 to 10^{-2} Hz at 30–80 °C. The ionic conductivity (σ) was determined from the following formula:

$$\sigma = \frac{L}{S{\cdot}R}$$

where L is the thickness of the film, S is the conducting area, and R is the resistance. The linear sweep voltammetry (LSV) tests were applied by a CHI660E electrochemical workstation in the asymmetric Li/SPE/SS cells with a scan rate of 1 mV/s at 30 °C. Symmetric Li/SPE/Li cells were assembled to test the critical current density and cyclic stability. The Li ion transference number (τ_{Li}^+) was measured by time ampere method and AC impedance spectroscopy. A potential of 10 mV was applied for a polarization time of 30,000 s. According to the formula:

$$\tau_{Li^+} = I_{ss}(\Delta V - I_0R_0)/I_0(\Delta V - I_{SS}R_{SS})$$

where I_0, ΔV and I_{SS} were initial state current, 10 mV polarization potential and steady-state current, respectively. R_0 and R_{SS} were the resistances at the start and completing time, respectively. All-solid-state metallic lithium batteries of $LiFePO_4$/SPE/Li were also assembled using $LiFePO_4$ electrodes and Li foils as cathodes and anodes, respectively. The active $LiFePO_4$ content of the electrodes was about 2.0 mg/cm^2. The cathodes were prepared using 80 wt% $LiFePO_4$, 10 wt% PVDF, 9.7 wt% carbon black and 0.3 wt% multi-walled carbon nanotubes [9]. The Land CT2001A system was used to verify the battery performance in a potential range of 2.5–4.1 V at different C rates (1C = 170 mAh/g) at 30 °C.

3. Results and discussion

3.1. Dispersibility of the BN nanosheets

The dispersibility of the nanoparticles in the solvents has an important impact on the CPE properties, and thus the BN dispersibility in different solvents was firstly investigated. The dynamic light scattering (DLS) measurements showed that the average size of the BN nanosheets was 800–1300 nm when 0.278 g BN was dispersed in 5 mL ACN. In comparison, the average size was detected to be 115 nm for the BN/NMP solution (Fig. 2a). The poly-dispersity index was only 0.56, indicating that the high dispersibility of the BN nanosheets in the NMP solvent. Optical images of the BN nanosheets in various solvents furtherly confirmed the better dispersibility of the NMP solvent (Fig. S1). However, the average size increased greatly when the BN content in the NMP solvent exceeded 0.278 g (Fig. 2b). Therefore, the CPEs were prepared

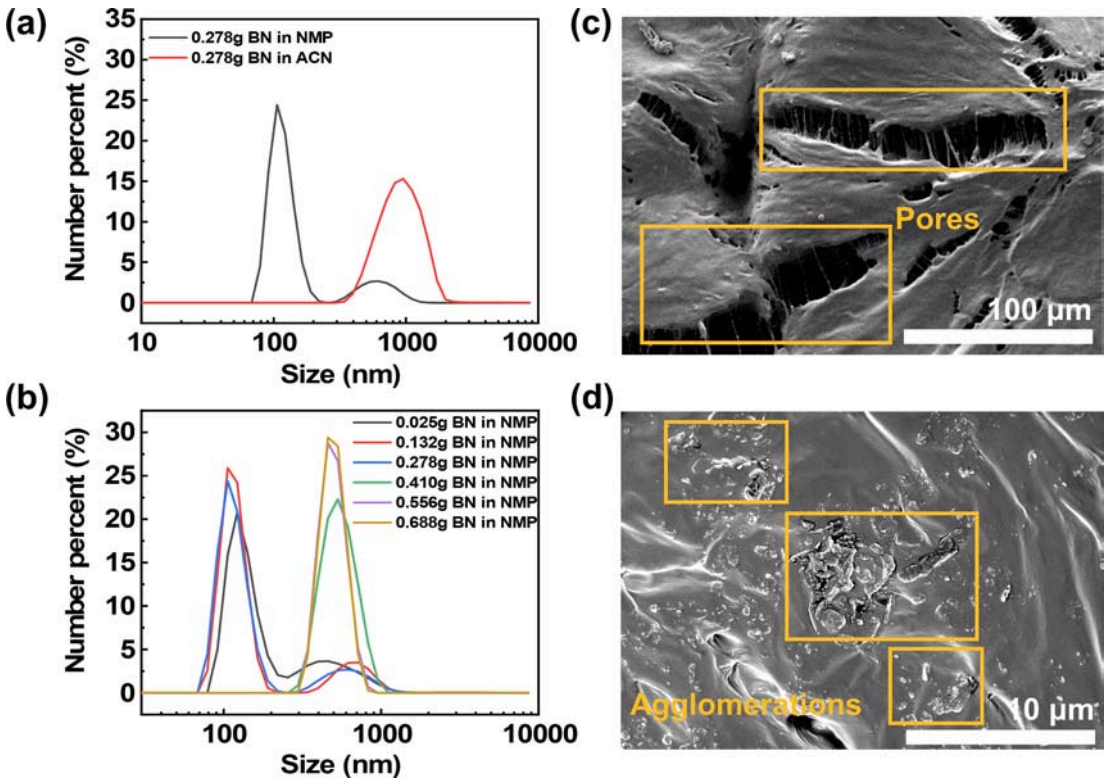

Fig. 2. (a) Size distribution of BN nanosheets in different solvents, and (b) size distribution of the BN nanosheets in NMP. SEM images of the (c) surface and (d) cross section of the CPE prepared using the BN-containing ACN solution.

using less than 0.278 g BN (i.e., 10 wt% BN of the CPEs) to avoid the BN agglomeration in the experiment.

To verify the important role of the solvent on the CPE morphology, the CPE films with 10 wt% BN nanosheets were also prepared using ACN as the dispersant of BN (Fig. 2c and d, Fig. 3e-i and S2). SEM characterizations showed that the BN nanosheets aggregate severely in the CPEs (Fig. 2d), and large pores formed at the surfaces (Fig. 2c). In contrast, the CPE film prepared using NMP as solvent did not show any agglomeration (Fig. 3i). A few pores generated on the surface of the BN10 CPEs, however, the number and size of the pores were much less than those of the ACN-resulted CPEs (Fig. S2b and Fig. 3e). It was also worth noting that the CPE membranes with $\geq$ 15 wt% BN nanosheets cannot be prepared because plenty of cracks generated. Thus, the BN-containing CPE films were prepared using NMP rather than the commonly-used ACN as the dispersant of BN in the following experiment.

3.2. Morphology and microstructure

The microstructure of the BN nanosheets was observed by TEM (Fig. 3a1). The size of the BN nanosheets was between 100–200 nm (consistent with the DLS results in Fig. 2a–b), and the nanosheets showed a single-layer structure (Fig. 3a2). High-resolution TEM images showed a clear lattice morphology of BN with a (1 0 0) lattice spacing of about 0.23 nm (Fig. 3a3) [13]. When the selected area electron diffraction (SAED) beam was aligned along the direction of [0001], the SAED showed hexagonal symmetric spots (Fig. 3a4), proving that the crystal structure of the BN nanosheets was hexagonal [32,33]. The EDS mapping also confirmed the nitrogen and boron elements of the BN nanosheets (Fig. S3).

The morphology of the BN-modified CPEs was uncovered by SEM. The BN0, BN1, BN5 and BN10 CPEs had relatively smooth surfaces, and no BN agglomerates were found at the cross sections (Fig. 3b-i), which was different from that of the CPEs prepared using ACN as solvent (Fig. 2c and d). The thickness of the CPEs was about 200–250 μm (Fig. 3f–i). The EDS mapping further verified the uniform distribution of the BN nanosheets in the BN10 electrolyte (Fig. S4), which would be helpful for improving the properties of the CPEs.

3.3. Ion conductance of the electrolytes

The ionic conductivities of the SPEs can be obtained by the EIS test (Fig. 4a, Fig. S5 and Table S1). The ionic conductivity of the BN0 electrolyte was 4.7×10^{-6} S/cm at 30 °C. With the incorporation of the BN nanosheets into the SPEs, the ionic conductivity of the BN1, BN5 and BN10 electrolytes increased to 9.9×10^{-6}, 1.7×10^{-5} and 2.0×10^{-5} S/cm (up to about quadruple that of the pristine electrolyte), respectively. When increasing the temperature, the crystalline phase of the polymer would change to be amorphous state, and the polymer chains and the ions would move fast, which further leads to an increase in the ionic conductivity of the electrolytes. The BN10 electrolyte still exhibited the highest ionic conductivity of 9.3×10^{-5} S/cm, which was much higher than those of the BN0 (1.3×10^{-5} S/cm), BN1 (4.5×10^{-5} S/cm) and BN5 (7.4×10^{-5} S/cm) electrolytes at 50 °C.

The XRD, DSC, FT-IR and ssNMR were further taken to reveal the influence mechanism of the BN nanosheets on the ionic conductivity of the electrolytes. Fig. 4b shows the XRD pattern of the BN and SPEs. The diffraction peaks at 2θ = 26.7°, 41.6°, 50.1°, 54.9°, and 76.1° were corresponded to the (0 0 2), (1 0 0), (1 0 2), (0 0 4), and (1 1 0) crystal planes of BN (JCPDS card ID: 45–0896). The strong peaks at 19° and 23° were related to the PEO crystallization peaks, meaning the high crystallization degree of the pure PEO at room temperature. The strength of these peaks greatly decreased in the BN0 electrolyte, suggesting that the PEO crystallinity reduced with the LiTFSI addition. No significant characteristic peaks of BN were found in the CPEs, which was due to the good dispersion of BN in the electrolytes and the coating by PEO, consistent with the SEM results. There was no significant change or shift of the characteristic peaks of the CPEs, nor did there appear a hybrid

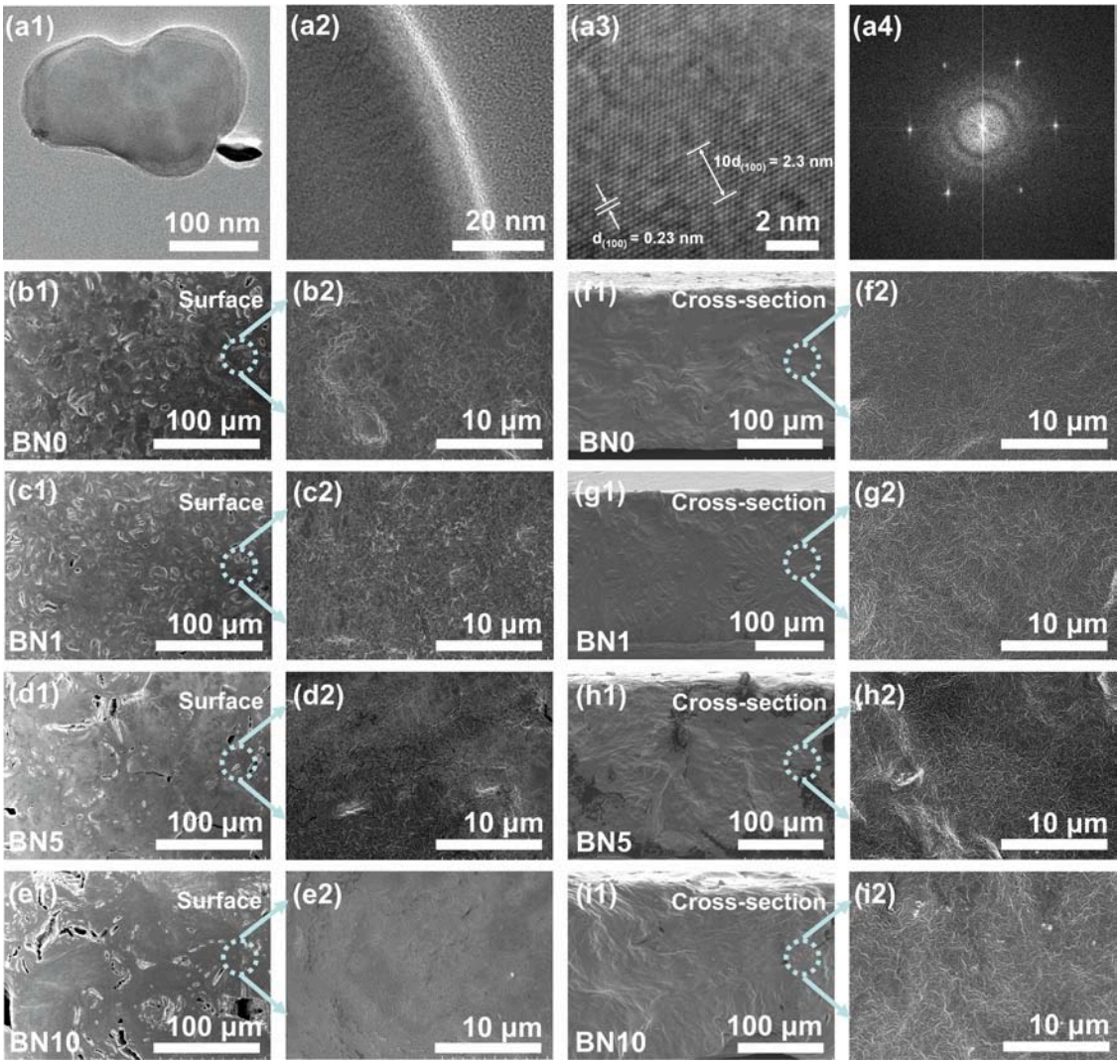

Fig. 3. (a1-a3) TEM images and (a4) selected area electron diffraction patterns of the BN nanosheets, (b1-b2, c1-c2, d1-d2 and e1-e2) surficial and (f1-f2, g1-g2, h1-h2 and i1-i2) cross-sectional SEM images of the (b1-b2 and f1-f2) BN0, (c1-c2 and g1-g2) BN1, (d1-d2 and h1-h2) BN5, and (e1-e2 and i1-i2) BN10 electrolytes.

peak after the BN filling, indicating that BN was stable in the polymer electrolytes without side chemical reactions. Moreover, compared with the PEO powder, the PEO peak intensity of the CPEs decreased gradually while filling BN, which proved that BN was beneficial for reducing the crystallinity of PEO.

The DSC measurements (Fig. 4c) further demonstrated that the crystallinity of the BN5 electrolyte was 30.9 %, which was lower than those of the PEO powder (83.1 %), and the BN0 (34.2 %) and BN1 (31.5 %) electrolytes. The crystallinity of the BN10 electrolyte reached 32.6 %, because of the high content filling. These results indicated that the BN nanoparticles played a plasticizing role in inhibiting the PEO crystallization, which was conducive to the polymer chain transport and the Li^+ migration along the polymer chains.

Fig. 4d and e showed the FTIR spectra of the BN, LiTFSI, PEO and SPEs in the scope of 4000–500 cm^{-1}. BN had obvious absorption peaks at 750 and 1270 cm^{-1}, corresponding to the bending vibration and tensile vibration modes of BN sp^2 bonding N − B − N bond, respectively [18,34]. The − OH peak at 3400 cm^{-1} represents the hydroxylation of the BN nanosheet surface [18]. PEO showed obvious triple C − O − C peaks at 1090 cm^{-1} [14], and double $-CH_2-$ peaks at 1340 cm^{-1} and 2880 cm^{-1} [5]. However, these peaks weakened or moved after adding LiTFSI. Moreover, the peak intensity of methylene at 2880 cm^{-1} decreased greatly after the addition of BN, which was due to the Lewis acid-base interaction between the electron deficient B atom and the polymer matrix [34]. This phenomenon also indicated a decrease of the crystalline region of the composite electrolytes, which was also demonstrated by the XRD and DSC measurements (Fig. 4b and c). LiTFSI had two tensile vibration peaks of the $-CF_3$ group at 747 and 774 cm^{-1}, and the characteristic peak of the S-O stretching at 608 cm^{-1} [9,14]. These three peaks moved to 740, 762 and 614 cm^{-1} in the BN0 electrolyte, respectively, due to the dissociation of LiTFSI and the coordination with PEO. They furtherly moved to 738, 760 and 617 cm^{-1} in the BN10 electrolyte, respectively, indicating that LiTFSI was greatly dissociated in the BN10 electrolyte. This should be due to the Lewis acid-base interaction between the BN and $TFSI^-$ anions especially the $-SO_2-$ groups, weakening the interaction between Li^+ and $TFSI^-$, which would facilitate the dissociation of LiTFSI and increase the content of free lithium ions. Because of the strong adsorption interaction between the BN and $TFSI^-$, the τ_{Li}^+ of BN1, BN5 and BN10 CPE are calculated to be 0.34, 0.41 and 0.33, which were much higher than that of the pristine BN0 SPE (0.18) (Fig. 4f and fig. S6). [35,36]. High τ_{Li}^+ would reduce the concentration polarization in the battery charge and discharge processes, drive the uniform deposition of Li^+, and prevent the undesirable side reactions on the electrodes [23].

DFT calculations and MD simulations were also taken to disclose the interaction between BN and $Li^+/TFSI^-$. The molecular structures were

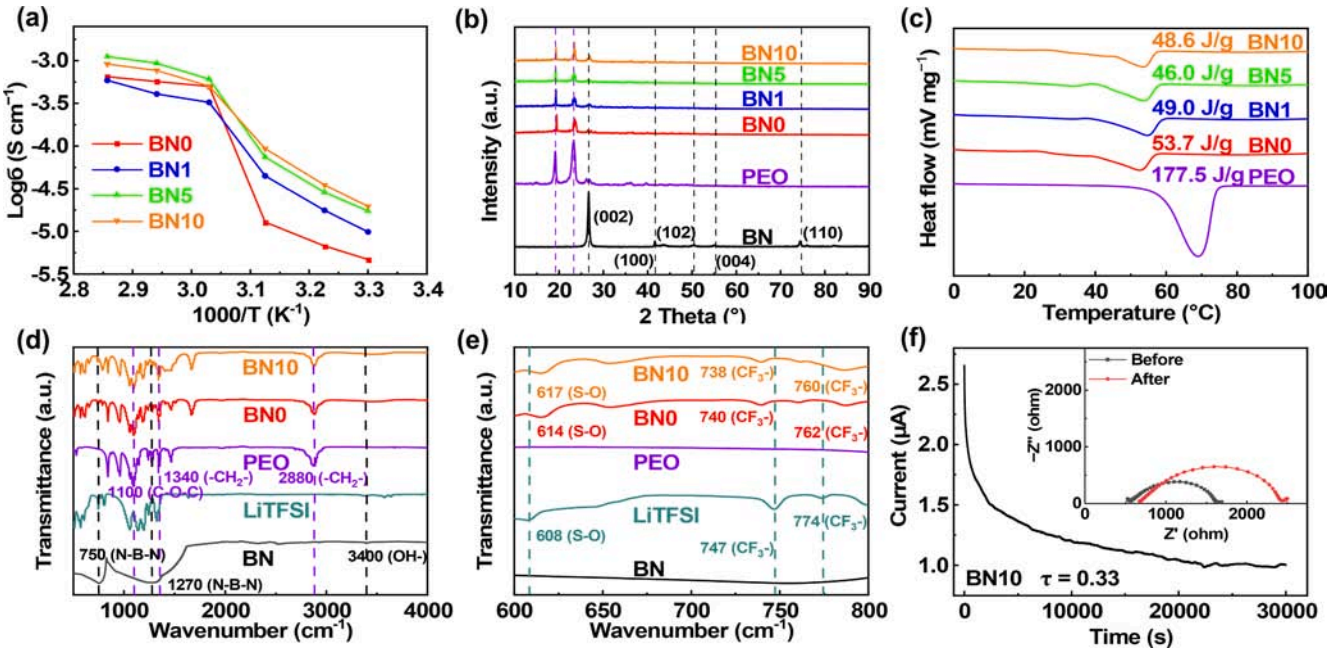

Fig. 4. (a) Ionic conductivity of the SPEs, (b) XRD patterns of the BN, PEO and SPEs, (c) DSC curves of the PEO and electrolytes, (d-e) FTIR spectra of the BN, LiTFSI, PEO and SPEs, and (f) the chronoamperometry (CA) curve for the BN10 electrolyte at 30 °C at 0.01 V (the inset is the EIS Nyquist chart before and after the polarization).

shown in Fig. 5a and b. After model cluster optimization, 12B atoms and 12 N atoms were used to build the BN molecular model, 2 − OH groups were connected to B atom, and the remaining unsaturated atoms were supplemented by H atom. It was found that the binding energy between $TFSI^-$ and BN was − 1.99 eV, which was lower than that of Li^+ and BN (−1.67 eV). The results showed that BN had stronger $TFSI^-$ adsorption ability than Li^+, which could promote the LiTFSI dissociation to generate more free Li^+, in good consistence to the FT-IR results (Fig. 4e).

Then the MD simulations were used to further investigate the effect of BN on ionic transportation in the SPEs (Fig. 5c and d). The ion diffusion coefficients can be estimated from the slope of the MSD curves (Fig. 5e and f). The simulation results showed that the diffusion coefficient of Li^+ in the BN10 system was 0.0046, which was larger than that in the BN0 system (0.0043). In addition, the diffusion coefficient of $TFSI^-$ decreased in the presence of BN (0.0057 vs 0.0049). These results proved that the filling of BN in the PEO-LiTFSI electrolytes can facilitate the transport of Li^+ and meanwhile inhibit the movement of $TFSI^-$, in agreement with the DFT calculations results. Thus, the introduction of

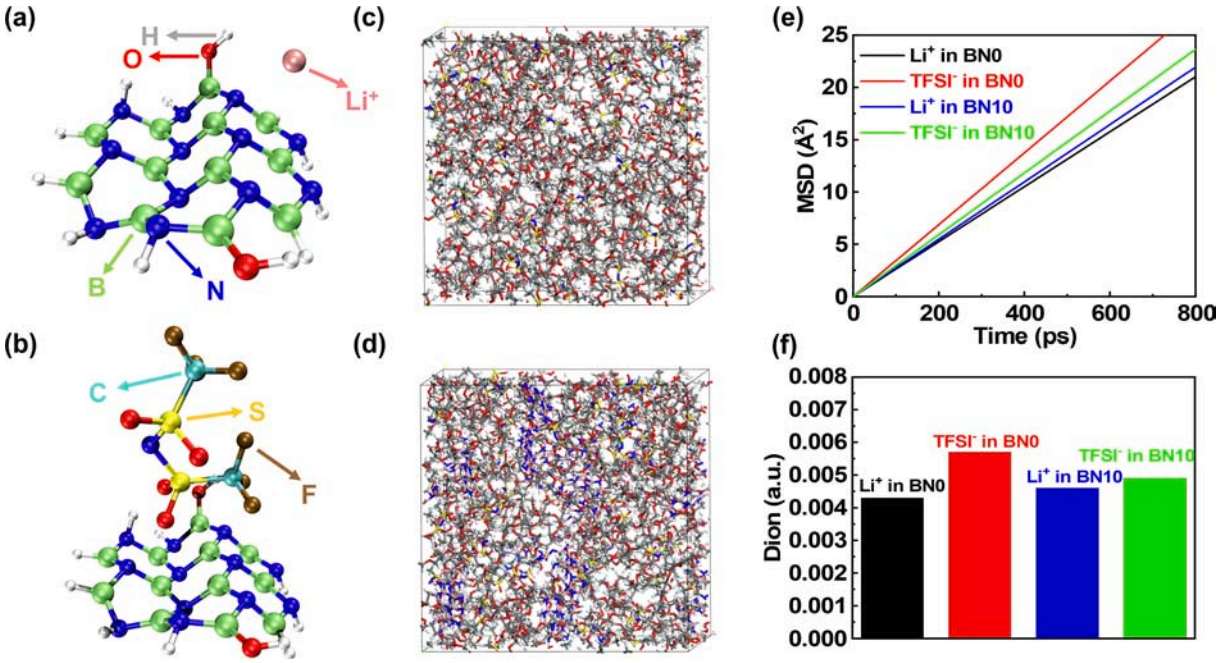

Fig. 5. The optimized configuration of (a) BN/Li^+ and (b) BN/$TFSI^-$. Pink: Li, red: O, white: H, green: B, blue: N, brown: F, indigo: C, yellow: S. Simulation model of Li^+ migration in (c) BN0 and (d) BN10 system, (e) the relationship between MSD and diffusion time of Li^+ and $TFSI^-$ in BN0 and BN10 systems, and (f) the diffusion coefficients of Li^+ and $TFSI^-$ in BN0 and BN10 systems. (For interpretation of the references to colour in this figure legend, the reader is referred to the web version of this article.)

BN into the electrolytes can increase τ_{Li}^{+} and the ionic conductivity of the CPEs.

As an effective tool to detect the environment and distribution of local ions in solids [37,38], ssNMR was also utilized to study the influence of BN on the Li^+ environment in the electrolytes (Fig. S7). The BN0 electrolyte showed a strong ^{7}Li peak at − 0.1 ppm, which was related to the Li^+ transport in the PEO bulk. Compared to the BN0 electrolyte, the Li peak intensity decreased and the main peak shifted to − 0.4 ppm in the BN5 electrolyte, suggesting a looser coordination between PEO and Li^+ [35] and an additional fast Li^+ pathway at the BN/PEO-LiTFSI interfaces, because of the Lewis acid-base interaction and the resulted abundant Li^+ ions at the interfaces and facilitated polymer segment movement in the amorphous phase. According to the aforesaid theoretical and experimental results, we can easily conclude that the increase of the ionic conductivity and the τ_{Li}^{+} of the BN-containing CPEs was attributed to the increase in the amorphous region of the polymer, the immobilization of the $TFSI^-$ to release more Li^+, and the formation of fast-ion pathways at the BN/PEO-LiTFSI interfaces.

3.4. Electrochemical, mechanical and thermal properties

In addition, as for the dendrite inhibition ability and the long-term cycle stability of the batteries, high electrochemical stability, mechanical strength and thermal stability are necessary for the CPEs. The decomposition voltage of the electrolytes was detected by the LSV test (Fig. 6a and Fig. S8). The oxidation potential of the BN0 electrolyte was ~ 4.4 V at 30 °C, which is similar to the previous report [39,40], and is also higher than that commonly tested at 60 °C (~3.9 V) [41]. In contrast, the electrochemical window of the BN-containing CPEs can reach ~ 5.0 V. The wider electrochemical window means that there are less oxidative decompositions during the charging/discharging processes, and the electrolytes can be matched with high-voltage cathode materials [42,43]. There are two main reasons for the improvement of the electrochemical window by the BN adding. First, BN can combine with the electrons on the O atoms in $TFSI^-$ to anchor the anions on the surface of BN nanosheets, which can inhibit the decomposition of LiTFSI. A few studies have shown that the decomposition of $TFSI^-$ would result in a narrow electrochemical window of the PEO-LiTFSI electrolyte [44]. In addition, the BN nanosheets with high chemical and electrochemical stabilities were uniformly dispersed in the PEO matrices would also contribute to the electrochemical stability of the CPEs.

The stress–strain test of the films was conducted to detect the ability of the SPEs to inhibit lithium dendrites. As is shown in Fig. 6b, the ultimate tensile strength and Young's modulus of the pristine BN0 electrolyte were 0.85 MPa and 0.72 MPa, respectively, which were consistent with the relevant reports [14,45]. In sharp contrast, the tensile strength and Young's modulus of the BN10 electrolyte increased to 2.62 and 2.91 MPa, respectively, much higher than those of the pristine BN0 electrolyte. These results indicated that the CPEs containing BN have high modulus to inhibit the lithium dendrites, which is conducive to prolong the battery life [14].

Fig. 6c shows the TGA curves of the BN, and the BN0, BN1, BN5 and BN10 electrolytes. The electrolytes had a slight mass loss of ~ 3.5 % up to 135 °C (the temperature of all the free solvents completely evaporate) [46], indicating that there was little free solvent in the SPEs. In addition, solvated molecules of $[Li(NMP)_x]^+$ may be formed because of the strong interaction between LiTFSI and NMP, which would lead an increase of the decomposition temperature. The additional weight loss of 2.5–3.5 % during the temperature range of 135–160 °C should be ascribed to the evaporation of the solvated NMP and the decomposition of LiTFSI [46,47]. Another obvious weightlessness phenomena occurred at ~ 390 °C due to the decomposition of PEO [48]. The BN10 and BN0 electrolytes remained 10 % and 0 % at 700 °C, and the difference was consistent with the BN content in the CPEs. The mass of the BN nanosheets did not change up to 700 °C, which indicated the high thermal stability of the BN nanocrystals again. Fig. 6d shows the optical photos

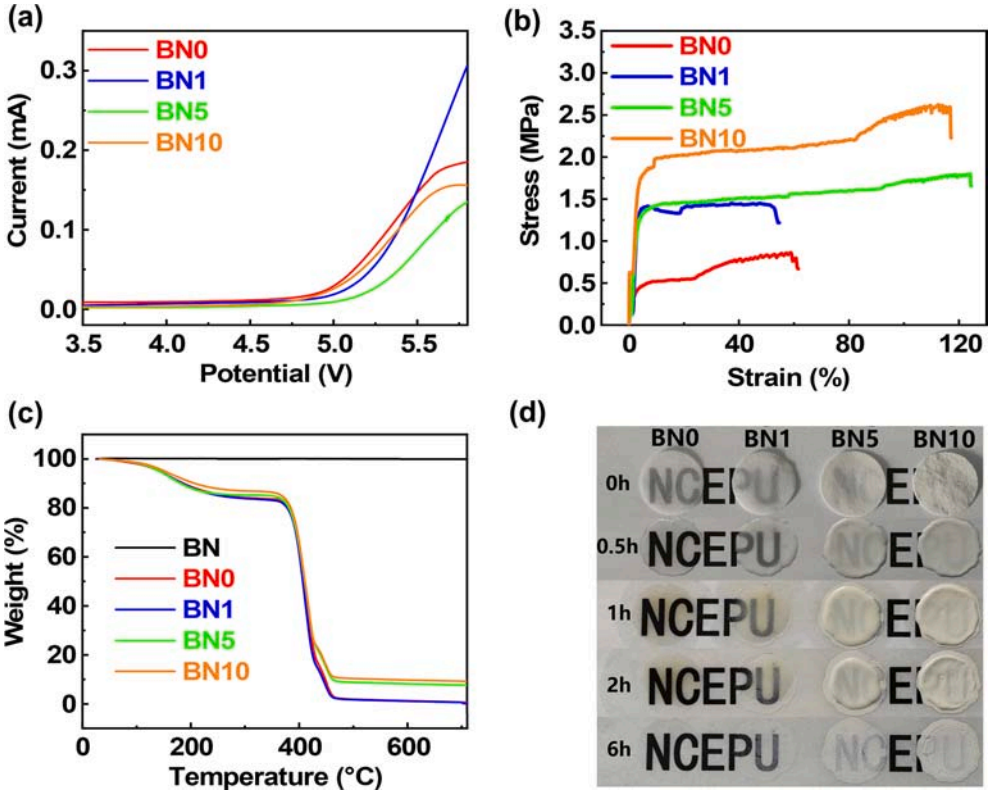

Fig. 6. (a) The LSV curves of BN and different SPEs, (b) mechanical property and (c) TGA curves of the SPEs, and (d) optical pictures at 140 °C for different time of the BN0, BN1, BN5 and BN10 electrolyte membranes.

of the electrolytes at 140 °C for different time. The BN0 electrolyte turned yellow and melted after 1 h. In contrast, the BN5 and BN10 electrolyte discs always maintained their original morphology and had no obvious change after 6 h, indicating the enhanced thermal stability of the CPEs than the BN0 electrolyte by the BN nanosheet filling.

The flame retardancy of the electrolytes was determined by a direct ignition test (Fig. S9). The BN0 electrolyte film can be easily ignited after 2 s when contacting with the flame, and then burned autonomously. On the contrary, it was difficult to ignite the BN10 electrolyte film, and self-extinguishing phenomenon can be observed, which indicated that BN greatly improved the flame retardance of the CPEs. These results indicated that filling high-thermostability BN nanosheets will effectively elevate the thermal stability of the electrolytes, which could effectively reduce the possibility of combustion and explosion, so as to achieve a safe, long cycle battery.

3.5. Lithium dendrite resistance

To verify the inhibition ability of the lithium dendrites by the composite electrolytes, the Li/SPE/Li symmetric cells were performed by gradually increasing current densities at 30 °C to test the critical current density (CCD) (Fig. 7a–d). Lithium ions were continuously plating/stripping on the lithium electrodes during the charging/discharging processes. The pristine BN0 electrolyte-based cells had a low CCD of only 0.10 mA/cm^2 with an areal capacity of 0.10 mAh/cm^2(the potential quickly reached 500 mV). In contrast, the potentials of the BN1, BN5 and BN10 electrolyte-based cells under the same conditions were only 340, 320 and 300 mV, respectively, and the CCDs were 0.15 mA/cm^2 with a high areal capacity of 0.15 mAh/cm^2. The lower the polarization voltage means more stability of the electrolyte/electrode interface [49]. The abovementioned results revealed that the BN filling can improve the stability of the interface contact and increase the ion transport capacity of the electrolytes, thus realizing the high current charging and discharging of the batteries.

The durability of the electrolyte membrane-based Li/Li cells was determined using the current density of 0.05 mA/cm^2 and the areal capacity of 0.05 mAh/cm^2 at 30 °C. The first three circles were cycled at a low current density (0.025 mA/cm^2) to obtain a stable interface. The initial overpotential of the BN0 electrolyte-based battery was about 380 mV, but the potential increased sharply to 5 V after 130 h (Fig. 7e). In comparison, the cells using the BN1 and BN5 electrolytes can cycle up to 210 and 450 h, respectively (Fig. 7f–g). The BN10 electrolyte-based battery almost maintained the original potential of about 300 mV during the whole cycle, and can steadily run for 1200 h without short circuit (Fig. 7h). This excellent cycle performance is better than the most reported Li/Li symmetric batteries using the nanoparticle-filled PEO electrolytes at room temperature or even at high-temperatures (Table S2). This should be attributed to the BN filling in the electrolytes. On the one hand, the improvement of the mechanical strength (especially the Young's modulus) of the CPEs by BN was helpful for

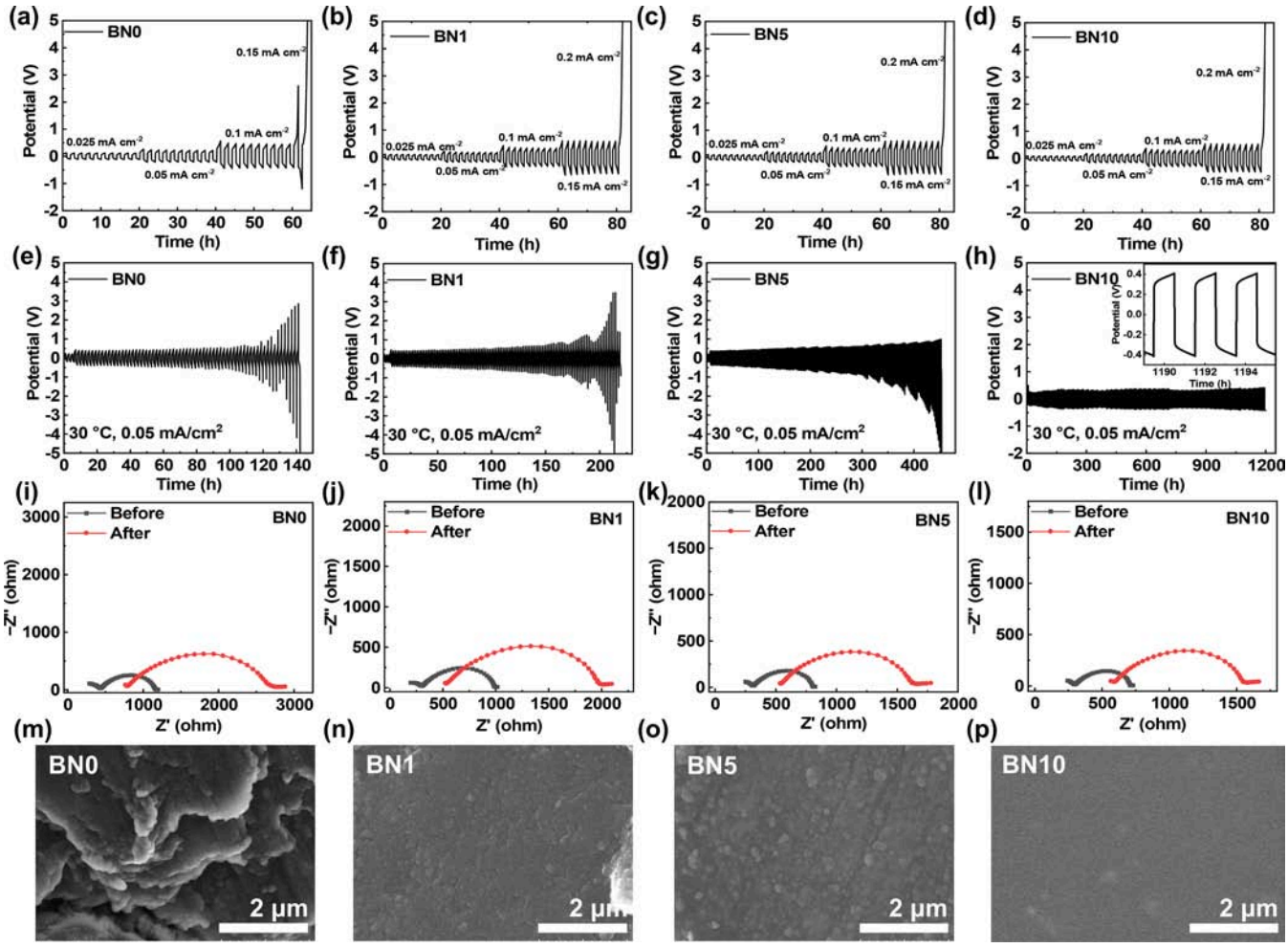

Fig. 7. Critical current density test of the (a) BN0, (b) BN1, (c) BN5 and (d) BN10 electrolyte-based Li/Li symmetric cells at 30 °C; Voltage profiles of the (e) BN0, (f) BN1, (g) BN5 and (h) BN10 electrolyte-based Li/Li symmetric cells in the stripping/plating processes under 0.05 mA/cm^2 at 30 °C; EIS plots of the cells using the (i) BN0, (j) BN1, (k) BN5 and (l) BN10 electrolytes before and after the cycling; SEM images of the cycled Li anode surface using the (m) BN0, (n) BN1, (o) BN5 and (p) BN10 electrolyte membranes.

inhibiting the lithium dendrite formation (Fig. 6b), according to the Monroe-Newman theory [50,51]. On the other hand, according to Sand's Time theory [52], the time for Li^+ to be completely consumed near the lithium electrode (the time for the growing of lithium dendrites) is proportional to the τ_{Li}^{+}, and thus, the BN-containing CPEs with higher τ_{Li}^{+} can inhibit the dendrite growth more effectively than the pristine BN-free electrolyte.

The EIS tests were then conducted to reveal the changes of the battery impedance during the cycling processes (Fig. 7i–l). The semicircles in the high-frequency region and low-frequency region in the Nyquist diagram were attributed to the ohmic resistance (R_e) of the SPE and the interfacial resistance (R_i) between the SPE and the lithium electrode, respectively [9,14]. The BN0 electrolyte-based cell exhibited high R_e and R_i of 427 and 737 Ω before the charge–discharge cycling, respectively. And the resistances increased to 780 and 1989 Ω after the cycling, respectively. The increasing impedance of the electrolyte and interface can be due to the depletion of electrolyte side reactions under the high voltage and the continuous accumulation of "dead lithium" [53]. In comparison, the R_e and R_i of the BN10 electrolyte-based cell were 294 and 420 Ω before the cycling, and only increased to 589 and 971 Ω after the cycling, respectively. These results indicated that the BN filling can reduce the electrolyte resistance and have the prominent interfacial compatibility against Li dendrite.

The surface morphology changes of the lithium metal before and after the cycling were then revealed by using SEM (Fig. 7m–p and Fig. S10). As is shown in Fig. S10, the surface of the lithium metal electrode before the cycling was smooth. But a lot of layered lichen-like lithium dendrites appeared on the lithium electrodes in the BN0 electrolyte-based batteries after the cycling, and holes and cracks also generated. In stark contrast, the surface of the cycled lithium electrodes in the BN1, BN5 and BN10 electrolyte-based batteries was relatively flat, and the lithium deposition was more uniform and denser. SEM characterization of the cycled electrolytes also revealed that the BN nanosheets in CPEs can greatly inhibit the formation of lithium dendrites (Fig S11a–d). The pristine BN0 electrolyte membrane was covered with a lot of crushed lithium deposits. However, the surfaces of the BN1, BN5 and BN10 electrolytes were flat, and no obvious lithium dendrites were found. This once again verified that the BN nanosheets in the CPEs can greatly facilitate the uniform deposition of lithium and inhibit the dendrite growth.

3.6. Metallic lithium battery cycling performance at room temperature

As mentioned above the BN nanosheets greatly improved the comprehensive properties of the electrolytes, such as the ionic conductivity, electrochemical window, mechanical strength, thermal stability, and the interfacial stability against Li dendrites. To investigate the practical application in metallic lithium batteries at room temperature, the $LiFePO_4$/SPE/Li batteries were assembled and tested at 30 °C at different rates (Fig. 8a). The batteries based on the BN10 electrolyte showed higher discharge capacities of 165, 153, 128 and 67 mAh/g than those based on the BN0 (128, 115, 79 and 38 mAh/g), BN1 (147, 133, 96 and 43 mAh/g) and BN5 (151, 136, 98 and 44 mAh/g) electrolytes at 0.1, 0.2, 0.3 and 0.5C, respectively. When the current density returned again to 0.1C after 25cycles, the BN10 electrolyte-based battery still maintained a high capacity of 167 mAh/g, which was also much higher than other batteries. The capacity increasing at the first 5cycles was due to the activation process of the $LiFePO_4$ electrode and the improved physical contact at the interface between the electrolytes and the electrodes. In addition, the CPE-based batteries exhibited the narrow charge–discharge platforms at different rates than those of BN0-based battery (Fig. 8b–c and Fig. S12), and the voltage polarization was relatively lower, which also reflects that $LiFePO_4$/CPE/Li batteries have more stable compatibility and enhanced ion dynamics [54].

The $LiFePO_4$/SPE/Li cells were conducted at 0.3C and 30 °C to test the long-term cycling performance (Fig. 8d–f, Fig. S13 and Fig. S14). The capacity of the pristine BN0 electrolyte-assembled $LiFePO_4$/Li battery rapidly dropped from 88 mAh/g to 27 mAh/g with a capacity retention of 29 % after 90 cycles. In stark contrast, the BN10 electrolyte-based battery with an initial capacity of 132 mAh/g maintained 111 mAh/g after 90 cycles with a high capacity-retention of 84 %. The capacities of the BN1 and BN5 electrolyte-based batteries decreased from 118 and

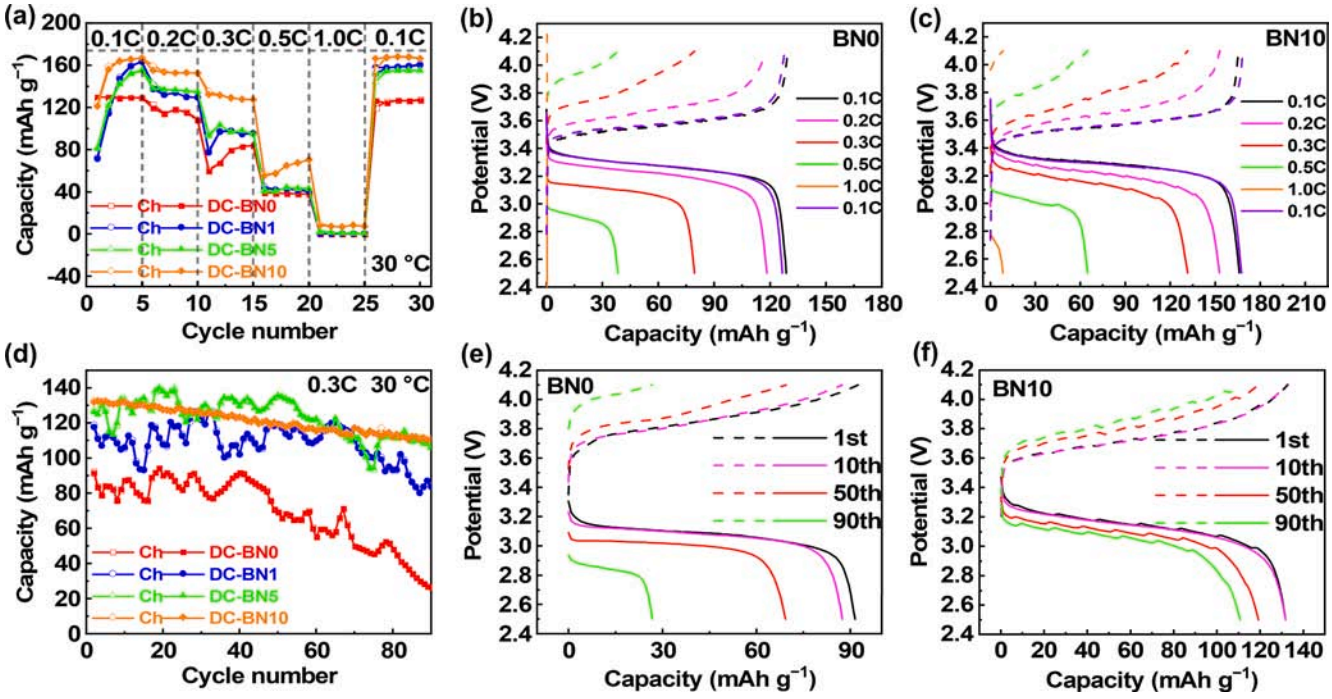

Fig. 8. (a) Rate capability of the solid-state $LiFePO_4$/Li cells at 30 °C, and the corresponding charge–discharge profiles of the (b) BN0 and (c) BN10 electrolyte-based cells at various C rates; (d) Long-term cycling performance of the $LiFePO_4$/Li cells at 0.3C and 30 °C, and the corresponding charge–discharge profiles of the (e) BN0 and (f) BN10 electrolyte-based cells.

126 mAh/g to 84 and 106 mAh/g with capacity retentions of 73 % and 84 %, respectively. We also found the capacity variation during the whole cycling process, which may be ascribed to the oxidization of the terminal –OH groups of PEO and the formation of –COOH (Li) and Li_2O [55–57]. We will explore the reason of this phenomenon in the future work.

Table S2 summarizes the cycling performance and capacity of the recently-reported PEO-LiTFSI based solid-state cells. At present, there are few PEO-based electrolytes meeting the needs of all-solid-state metallic lithium batteries at room temperature. Compared with other articles, the BN-containing cells still showed the more stable long-term cycle performance and much higher capacity at high charge/discharge rate (0.3C) and room temperature (30 °C). It was also worth mentioning that all the batteries showed high Coulomb efficiencies (~100 %) over the 90 cycles (Fig. S15), which was much higher than that of the liquid electrolyte-based batteries. During the 90 cycles, the batteries using the BN10 electrolyte also showed a higher average discharge voltage of 3.06 V than the BN5, BN1 and BN0 electrolyte-based cells (3.01, 2.91 and 2.84 V).

The impedance changes of the $LiFePO_4$/Li batteries before and after the cycling were also measured (Fig. S16, Table S3). The semicircle of the high frequency region and the point of intersection with the real axis were related to the charge transfer resistance (R_{ct}) and the ohmic resistance (R_e), respectively [9,58]. As shown in Table S3, the high-modulus BN filling in the PEO matrices would affect the interfacial contact between the electrolyte and the electrodes, and thus the BN-containing cells had higher R_e values than the BN-free cells, in spite of the much higher ionic conductivity of the BN-filled electrolytes. However, the R_e and R_{ct} of the BN0 electrolyte-based Li/$LiFePO_4$ batteries increased greatly from 591 and 471 Ω to 1379 and 3251 Ω after 90 cycles, respectively, which were much higher than those of the BN10 electrolyte-based batteries (1236 and 1791 Ω). This confirmed the positive effect of the BN nanosheets on the CPEs once again (e.g., the electrochemical window and the resistance against the dendrite growth).

Solid-state $LiNi_{0.6}Co_{0.2}Mn_{0.2}O_2$/Li batteries were also assembled and cycled at 30 °C within 2.8–4.3 V to confirm the stability of CPEs with high-voltage cathodes (Fig. S17). The BN0 electrolyte-based $LiNi_{0.6}Co_{0.2}Mn_{0.2}O_2$/Li battery showed low capacities of 94 and 59 mAh/g at 0.05C and 0.1C, respectively. In stark contrast, the BN-containing $LiNi_{0.6}Co_{0.2}Mn_{0.2}O_2$/Li batteries displayed much higher capacities of 139 and 113 mAh/g at 0.05C and 0.1C, respectively, and the capacity remained 135 mAh/g when cycled at 0.05C again. In addition, the BN-containing batteries showed much higher capacity and cycling stability in the long-term cycling process, compared to the BN0 electrolyte-based battery. This further proved the positive effect of the BN filling on the high-voltage batteries.

In summary, compared with the pristine BN0 electrolyte-based battery, the BN-containing batteries showed better rate performance and long-term cycling stability at room temperature. Specifically, the high ionic conductivity and τ_{Li}^{+} of the CPEs filled with the well-dispersed BN nanosheets are conducive to the acceleration of lithium ion reaction kinetics and the regulation of the Li^+ flux. The wide electrochemical window ensures high electrochemical stability, and the high Young's modulus and good Li dendrite inhibition further ensure the interfacial stability during the cycle.

4. Conclusions

The BN nanosheets were utilized as multifunctional nanofillers for preparing PEO-based CPEs to improve the cycling performance of room-temperature metallic lithium batteries. The high-content BN nanosheets with well dispersion in the PEO matrix can effectively inhibit the crystallization of PEO and capture $TFSI^-$ to release more free lithium ions. Together with the formation of fast-ion BN/PEO-LiTFSI interfaces, the ionic conductivity and τ_{Li}^{+} of the CPE membranes greatly increased to 4 and 2 times those of the pristine electrolyte at room temperature. Compared to the pristine BN0 electrolyte, the electrochemical window, Young's modulus and thermal stability of the electrolytes were also significantly enhanced with the addition of the BN nanosheets. Because of these improved properties, the CPE-based Li/Li cells can stably cycle for 1200 h at 0.05 mA/cm^2 (0.05 mAh/cm^2). The $LiFePO_4$/CPE/Li batteries also delivered higher rate performance and cycling stability (84 % capacity retention after 90 cycles at 0.3C) at room temperature. This research provides a novel way to prepare comprehensively-updated polymer electrolytes with high-content nanofillers for room-temperature all-solid-state metallic lithium batteries.

Declaration of competing interest

The authors declare that they have no known competing financial interests or personal relationships that could have appeared to influence the work reported in this paper.

Data availability

Data will be made available on request.

Acknowledgements

This work is supported partially by the Hebei Natural Science Foundation (E2022502022), the National Natural Science Foundation of China (52272200, 51972110, 52102245, 52072121), the project of State Key Laboratory of Alternate Electrical Power System with Renewable Energy Sources (LAPS21004), the Beijing Science and Technology Project (Z211100004621010), the Beijing Natural Science Foundation (2222076, 2222077), the Huaneng Group Headquarters Science and Technology Project (HNKJ20-H88), the Fundamental Research Funds for the Central Universities (2021MS028, 2020MS023, 2020MS028), and the NCEPU "Double First-Class" Program.

Appendix A. Supplementary data

Supplementary data to this article can be found online at https://doi.org/10.1016/j.apsusc.2023.158962.

References

[1] D. Li, H. Wang, H.K. Liu, Z. Guo, A new strategy for achieving a high performance anode for lithium ion batteries—Encapsulating germanium nanoparticles in carbon nanoboxes, Adv Energy Mater. 6 (2016) 1501666–1501671.
[2] D. Zhang, X. Meng, W. Hou, W. Hu, J. Mo, T. Yang, et al., Solid polymer electrolytes: Ion conduction mechanisms and enhancement strategies, Nano Res Energy. 2 (2023) 9120050–9120093.
[3] D.M. Reinoso, M.A. Frechero, Strategies for rational design of polymer-based solid electrolytes for advanced lithium energy storage applications, Energy Storage Mater. 52 (2022) 430–464.
[4] O. Sheng, C. Jin, J. Luo, H. Yuan, C. Fang, H. Huang, et al., Ionic conductivity promotion of polymer electrolyte with ionic liquid grafted oxides for all-solid-state lithium–sulfur batteries, J Mater Chem A. 5 (2017) 12934–12942.
[5] O. Sheng, C. Jin, J. Luo, H. Yuan, H. Huang, Y. Gan, et al., $Mg_2B_2O_5$ nanowire enabled multifunctional solid-state electrolytes with high ionic conductivity, excellent mechanical properties, and flame-retardant performance, Nano Lett. 18 (2018) 3104–3112.
[6] Z. Zhang, R.G. Antonio, K.L. Choy, Boron nitride enhanced polymer/salt hybrid electrolytes for all-solid-state lithium ion batteries, J Power Sources. 435 (2019) 226736–226744.
[7] L. Yue, J. Ma, J. Zhang, J. Zhao, S. Dong, Z. Liu, et al., All solid-state polymer electrolytes for high-performance lithium ion batteries, Energy Storage Mater. 5 (2016) 139–164.
[8] Y. Zheng, Y. Yao, J. Ou, M. Li, D. Luo, H. Dou, et al., A review of composite solid-state electrolytes for lithium batteries: Fundamentals, key materials and advanced structures, Chem Soc Rev. 49 (2020) 8790–8839.
[9] L. Liu, J. Mo, J. Li, J. Liu, H. Yan, J. Lyu, et al., Comprehensively-modified polymer electrolyte membranes with multifunctional PMIA for highly-stable all-solid-state lithium-ion batteries, J Energy Chem. 48 (2020) 334–343.
[10] R. Fang, B. Xu, N.S. Grundish, Y. Xia, Y. Li, C. Lu, et al., Li_2S_6-Integrated PEO-based polymer electrolytes for all-solid-state lithium-metal batteries, Angew Chem Int Ed. 60 (2021) 17701–17706.

[11] J. Mohanta, D.K. Padhi, S. Si, Li-ion conductivity in PEO-graphene oxide nanocomposite polymer electrolytes: A study on effect of the counter anion, J Appl Polym Sci. 135 (2018) 46336–46345.
[12] M. Yuan, J. Erdman, C. Tang, H. Ardebili, High performance solid polymer electrolyte with graphene oxide nanosheets, RSC Adv. 4 (2014) 59637–59642.
[13] Y. Li, L. Zhang, Z. Sun, G. Gao, S. Lu, M. Zhu, et al., Hexagonal boron nitride induces anion trapping in a polyethylene oxide based solid polymer electrolyte for lithium dendrite inhibition, J Mater Chem A. 8 (2020) 9579–9589.
[14] L. Liu, J. Lyu, J. Mo, H. Yan, L. Xu, P. Peng, et al., Comprehensively-upgraded polymer electrolytes by multifunctional aramid nanofibers for stable all-solid-state Li-ion batteries, Nano Energy 69 (2020) 104398–104408.
[15] W. Tang, S. Tang, C. Zhang, Q. Ma, Q. Xiang, Y.W. Yang, et al., Simultaneously enhancing the thermal stability, mechanical modulus, and electrochemical performance of solid polymer electrolytes by incorporating 2D sheets, Adv Energy Mater. 8 (2018) 1800866–1800872.
[16] J. Xu, Y. Meng, Q. Ding, R. Wang, T. Gan, J. Zhang, et al., High performance lithium ion electrolyte based on a three-dimensional holey graphene framework cross-linked with a polymer, J Mater Chem A. 10 (2022) 4402–4407.
[17] D. Lin, P.Y. Yuen, Y. Liu, W. Liu, N. Liu, R.H. Dauskardt, et al., A silica-aerogel-reinforced composite polymer electrolyte with high ionic conductivity and high modulus, Adv Mater. 30 (2018) 1802661–1802668.
[18] H. An, Q. Liu, J. An, S. Liang, X. Wang, Z. Xu, et al., Coupling two-dimensional fillers with polymer chains in solid polymer electrolyte for room-temperature dendrite-free lithium-metal batteries, Energy Storage Mater. 43 (2021) 358–364.
[19] Z. Sun, Y. Li, S. Zhang, L. Shi, H. Wu, H. Bu, et al., g-C_3N_4 nanosheets enhanced solid polymer electrolytes with excellent electrochemical performance, mechanical properties, and thermal stability, J Mater Chem A. 7 (2019) 11069–11076.
[20] Q. Pan, Y. Zheng, S. Kota, W. Huang, S. Wang, H. Qi, et al., 2D MXene-containing polymer electrolytes for all-solid-state lithium metal batteries, Nanoscale Adv. 1 (2019) 395–402.
[21] L. Liu, J. Lyu, J. Mo, P. Peng, J. Li, B. Jiang, et al., Flexible, high-voltage, ion-conducting composite membranes with 3D aramid nanofiber frameworks for stable all-solid-state lithium metal batteries, Sci China Mater. 63 (2020) 703–718.
[22] D. Lin, W. Liu, Y. Liu, H.R. Lee, P.C. Hsu, K. Liu, et al., High Ionic conductivity of composite solid polymer electrolyte via in situ synthesis of monodispersed SiO2 nanospheres in poly(ethylene oxide), Nano Lett. 16 (2016) 459–465.
[23] Q. Wang, J.-F. Wu, Z.-Y. Yu, X. Guo, Composite polymer electrolytes reinforced by two-dimensional layer-double-hydroxide nanosheets for dendrite-free lithium batteries, Solid State Ion. 347 (2020) 115275–115281.
[24] H. Xu, P.H. Chien, J. Shi, Y. Li, N. Wu, Y. Liu, et al., High-performance all-solid-state batteries enabled by salt bonding to perovskite in poly(ethylene oxide), P Natl Acad Sci USA 116 (2019) 18815–18821.
[25] T. Yang, J. Zheng, Q. Cheng, Y.Y. Hu, C.K. Chan, Composite polymer electrolytes with $Li_7La_3Zr_2O_{12}$ garnet-type nanowires as ceramic fillers: mechanism of conductivity enhancement and role of doping and morphology, ACS Appl Mater Interfaces. 9 (2017) 21773–21780.
[26] J. Zheng, P. Wang, H. Liu, Y.-Y. Hu, Interface-Enabled ion conduction in Li10GeP2S12–Poly(ethylene oxide) hybrid electrolytes, ACS Appl Energ Mater. 2 (2019) 1452–1459.
[27] W. Liu, S.W. Lee, D. Lin, F. Shi, S. Wang, A.D. Sendek, et al., Enhancing ionic conductivity in composite polymer electrolytes with well-aligned ceramic nanowires, Nat Energy. 2 (2017) 17035–17043.
[28] J. Shim, H.J. Kim, B.G. Kim, Y.S. Kim, D.-G. Kim, J.-C. Lee, 2D boron nitride nanoflakes as a multifunctional additive in gel polymer electrolytes for safe, long cycle life and high rate lithium metal batteries, Energ Environ Sci. 10 (2017) 1911–1916.
[29] S.J. Xu, Z.H. Sun, C.G. Sun, F. Li, K. Chen, Z.H. Zhang, et al., Homogeneous and fast ion conduction of PEO-based solid-state electrolyte at low temperature, Adv Funct Mater. 30 (2020) 2007172–2007182.
[30] Z. Huang, W. Pang, P. Liang, Z. Jin, N. Grundish, Y. Li, et al., A dopamine modified $Li_{6.4}La_3Zr_{1.4}Ta_{0.6}O_{12}$/PEO solid-state electrolyte: enhanced thermal and electrochemical properties, J Mater Chem A. 7 (2019) 16425–16436.
[31] C. Hu, Y. Shen, M. Shen, X. Liu, H. Chen, C. Liu, et al., Superionic conductors via bulk interfacial conduction, J Am Chem Soc. 142 (2020) 18035–18041.
[32] K.H. Oh, D. Lee, M.J. Choo, K.H. Park, S. Jeon, S.H. Hong, et al., Enhanced durability of polymer electrolyte membrane fuel cells by functionalized 2D boron nitride nanoflakes, ACS Appl Mater Inter. 6 (2014) 7751–7758.
[33] D. Lee, S.H. Song, J. Hwang, S.H. Jin, K.H. Park, B.H. Kim, et al., Enhanced mechanical properties of epoxy nanocomposites by mixing noncovalently functionalized boron nitride nanoflakes, Small. 9 (2013) 2602–2610.
[34] M. Liu, S. Zhang, G. Li, C. Wang, B. Li, M. Li, et al., A cross-linked gel polymer electrolyte employing cellulose acetate matrix and layered boron nitride filler prepared via in situ thermal polymerization, J Power Sources. 484 (2021) 229235–229243.
[35] W. Bao, L. Zhao, H. Zhao, L. Su, X. Cai, B. Yi, et al., Vapor phase infiltration of ZnO quantum dots for all-solid-state PEO-based lithium batteries, Energy Storage Mater. 43 (2021) 258–265.
[36] Y. Liang, Y. Liu, D. Chen, L. Dong, Z. Guang, J. Liu, et al., Hydroxyapatite functionalization of solid polymer electrolytes for high-conductivity solid-state lithium-ion batteries, Mater Today Energy. 20 (2021) 100694–100702.
[37] J. Zheng, M.X. Tang, Y.Y. Hu, Lithium ion pathway within $Li_7La_3Zr_2O_{12}$-polyethylene oxide composite electrolytes, Angew Chem Int Ed. 55 (2016) 12538–12542.
[38] J. Zheng, Y.Y. Hu, New insights into the compositional dependence of Li-ion transport in polymer-ceramic composite electrolytes, Acs Appl Mater Interfaces. 10 (2018) 4113–4120.
[39] R. Fan, W.C. Liao, S.X. Fan, D.Z. Chen, J.N. Tang, Y. Yang, et al., Regulating interfacial Li-ion transport via an integrated corrugated 3D skeleton in solid composite electrolyte for all-solid-state lithium metal batteries, Adv Sci. 9 (2022) 2104506–2104516.
[40] J.Y. Yin, X. Xu, S. Jiang, H.H. Wu, L. Wei, Y.D. Li, et al., High ionic conductivity PEO-based electrolyte with 3D framework for Dendrite-free solid-state lithium metal batteries at ambient temperature, Chem Eng J. 431 (2022) 133352–133361.
[41] X. Wang, S.P. Huang, K. Guo, Y.L. Min, Q.J. Xu, Directed and continuous interfacial channels for optimized ion transport in solid-state electrolytes, Adv Funct Mater. 32 (2022) 2206976–2206988.
[42] C. Fu, S. Lou, X. Xu, C. Cui, C. Li, P. Zuo, et al., Capacity degradation mechanism and improvement actions for 4 V-class all-solid-state lithium-metal polymer batteries, Chem Eng J. 392 (2020) 123665–123672.
[43] Y. Jin, X. Zong, X. Zhang, Z. Jia, H. Xie, Y. Xiong, Constructing 3D Li+-percolated transport network in composite polymer electrolytes for rechargeable quasi-solid-state lithium batteries, Energy Storage Mater. 49 (2022) 433–444.
[44] K. Minami, F. Mizuno, A. Hayashi, M. Tatsumisago, Lithium ion conductivity of the Li_2S–P_2S_5 glass-based electrolytes prepared by the melt quenching method, Solid State Ion. 178 (2007) 837–841.
[45] Z. Zhang, Y. Huang, H. Gao, C. Li, J. Huang, P. Liu, 3D glass fiber cloth reinforced polymer electrolyte for solid-state lithium metal batteries, J Membrane Sci. 621 (2021) 118940–118951.
[46] P.B. Zhai, Z.L. Yang, Y. Wei, X.X. Guo, Y.J. Gong, Two-dimensional fluorinated graphene reinforced solid polymer electrolytes for high-performance solid-state lithium batteries, Adv Energy Mater. 12 (2022) 2200967–2200979.
[47] F. Xu, S. Deng, Q. Guo, D. Zhou, X. Yao, Quasi-ionic liquid enabling single-phase poly(vinylidene fluoride)-based polymer electrolytes for solid-state $LiNi_{0.6}Co_{0.2}Mn_{0.2}O_2$||Li batteries with rigid-flexible coupling interphase, Small Methods. 5 (2021) e2100262.
[48] S. Suriyakumar, S. Gopi, M. Kathiresan, S. Bose, E.B. Gowd, J.R. Nair, et al., Metal organic framework laden poly(ethylene oxide) based composite electrolytes for all-solid-state Li-S and Li-metal polymer batteries, Electrochim Acta. 285 (2018) 355–364.
[49] X. Guo, W. Peng, Y. Wu, H. Guo, Z. Wang, X. Li, et al., $Al_4B_2O_9$ nanorods-modified solid polymer electrolytes with decent integrated performance, Sci China Mater. 64 (2020) 296–306.
[50] C. Monroe, J. Newman, The effect of interfacial deformation on electrodeposition kinetics, J Electrochem Soc. 151 (2004) A880–A886.
[51] C. Monroe, J. Newman, The impact of elastic deformation on deposition kinetics at lithium/polymer interfaces, J Electrochem Soc. 152 (2005) A396–A404.
[52] J.S.S. Henry, On the concentration at the electrodes in a solution, with special reference to the liberation of hydrogen by electrolysis of a mixture of copper sulphate and sulphuric acid, Pro Phy Soc London. 17 (1899) 496–535.
[53] J. Li, L. Chen, F. Wang, Z. Qin, Y. Zhang, N. Zhang, et al., Anionic metal-organic framework modified separator boosting efficient Li-ion transport, Chem Eng J. 451 (2023) 138536–138544.
[54] W. Liu, C. Yi, L. Li, S. Liu, Q. Gui, D. Ba, et al., Designing polymer-in-salt electrolyte and fully infiltrated 3D electrode for integrated solid-state lithium batteries, Angew Chem Int Ed. 60 (2021) 12931–12940.
[55] X.F. Yang, M. Jiang, X.J. Gao, D. Bao, Q. Sun, N. Holmes, et al., Determining the limiting factor of the electrochemical stability window for PEO-based solid polymer electrolytes: main chain or terminal -OH group? Energ Environ Sci. 13 (2020) 1318–1325.
[56] J.W. Feng, J.Y. Wang, Q. Gu, W. Thitisomboon, D.H. Yao, Y.H. Deng, et al., Room-temperature all-solid-state lithium metal batteries based on ultrathin polymeric electrolytes, J Mater Chem A. 10 (2022) 13969–13977.
[57] W. Liu, G. Li, W. Yu, L. Gao, D. Shi, J. Ju, et al., Asymmetric organic-inorganic bi-functional composite solid-state electrolyte for long stable cycling of high-voltage lithium battery, Energy Storage Mater. 63 (2023) 103005–103016.
[58] L.H. Liu, D.M. Zhang, T.R. Yang, W.H. Hu, X.L. Meng, J.S. Mo, et al., Flexible ion-conducting membranes with 3D continuous nanohybrid networks for high-performance solid-state metallic lithium batteries, J Energy Chem. 75 (2022) 360–368.